NANO LETTERS

pubs.acs.org/NanoLett Letter

Conduction Band Replicas in a 2D Moiré Semiconductor Heterobilayer

Abigail J. Graham, Heonjoon Park, Paul V. Nguyen, James Nunn, Viktor Kandyba, Mattia Cattelan, Alessio Giampietri, Alexei Barinov, Kenji Watanabe, Takashi Taniguchi, Anton Andreev, Mark Rudner, Xiaodong Xu,* Neil R. Wilson,* and David H. Cobden*

Cite This: https://doi.org/10.1021/acs.nanolett.3c04866 **Read Online**

ACCESS | Metrics & More | Article Recommendations | Supporting Information

ABSTRACT: Stacking monolayer semiconductors creates moiré patterns, leading to correlated and topological electronic phenomena, but measurements of the electronic structure underpinning these phenomena are scarce. Here, we investigate the properties of the conduction band in moiré heterobilayers of WS_2/WSe_2 using submicrometer angle-resolved photoemission spectroscopy with electrostatic gating. We find that at all twist angles the conduction band edge is the **K**-point valley of the WS_2, with a band gap of 1.58 ± 0.03 eV. From the resolved conduction band dispersion, we deduce an effective mass of $0.15 \pm 0.02\ m_e$. Additionally, we observe replicas of the conduction band displaced by reciprocal lattice vectors of the moiré superlattice. We argue that the replicas result from the moiré potential modifying the conduction band states rather than final-state diffraction. Interestingly, the replicas display an intensity pattern with reduced 3-fold symmetry, which we show implicates the pseudo vector potential associated with in-plane strain in moiré band formation.

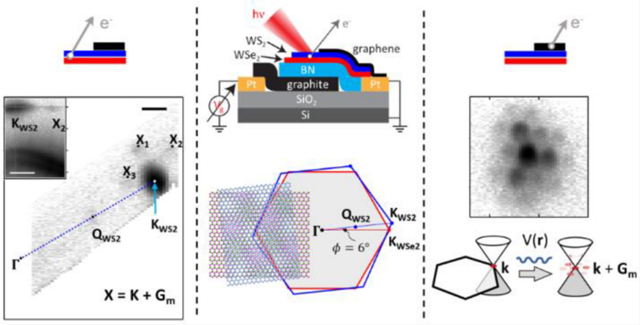

KEYWORDS: *Two-dimensional materials, two-dimensional heterostructures, two-dimensional semiconductors, angle-resolved photoemission spectroscopy*

The diverse ramifications of moiré superstructures formed in two-dimensional (2D) van der Waals heterostructures are of great current interest. Most famously, stacks of graphene sheets with appropriate rotational misalignment between the layers exhibit moiré superlattices that create nearly flat bands and lead to correlated insulating states, superconductivity, Chern insulators, and more.[1−4] The existence of these graphene moiré bands and of correlation-induced spectral gaps within them has been directly confirmed by submicrometer-scale angle-resolved photoemission spectroscopy[5,6] (μARPES) and scanning tunneling microscopy.[7,8]

Artificial bilayers of two-dimensional (2D) semiconductors also exhibit moiré superlattices[9,10] enabling the study of phenomena such as exciton arrays,[11−14] Mott insulating states and generalized Wigner crystals,[15,16] excitonic insulators,[17,18] tunable magnetism,[16,19,20] Kondo lattices,[21] and fractional quantum anomalous Hall states.[22−24] Although most attention to date has been paid to situations of hole-doping, where the action is in the valence bands, the conduction bands (CBs) play an important role in all optical measurements and they must also be affected by the moiré lattice. In this work, we use μARPES to probe the conduction band structure of 2D moiré semiconductors for the first time. ARPES detects only occupied states and so is normally limited to probing the valence bands,[25−27] but occupation of the conduction band can be induced by optical pumping[28,29] or electrostatic doping.[30] We follow the latter approach, incorporating a metallic gate electrode under the heterostructure, which allows electrostatic doping and thus detection of the CB edges[31] as well as changes in the bands resulting from doping[32−34] or electric field.[35]

We focus on WS_2/WSe_2 heterobilayers, where the moiré potential is known to be strong at small twist angles,[16,36] presenting data collected from three devices with different twist angles. We find that the band alignment of the separate monolayers is maintained independently of the twist angle, and we determine the band gap, make the first measurement of the CB effective mass, and observe perturbing effects of the moiré potential on the CB that manifest as multiple replicas of the original CB displaced by reciprocal lattice vectors of the moiré

Received: December 12, 2023
Revised: April 11, 2024
Accepted: April 11, 2024

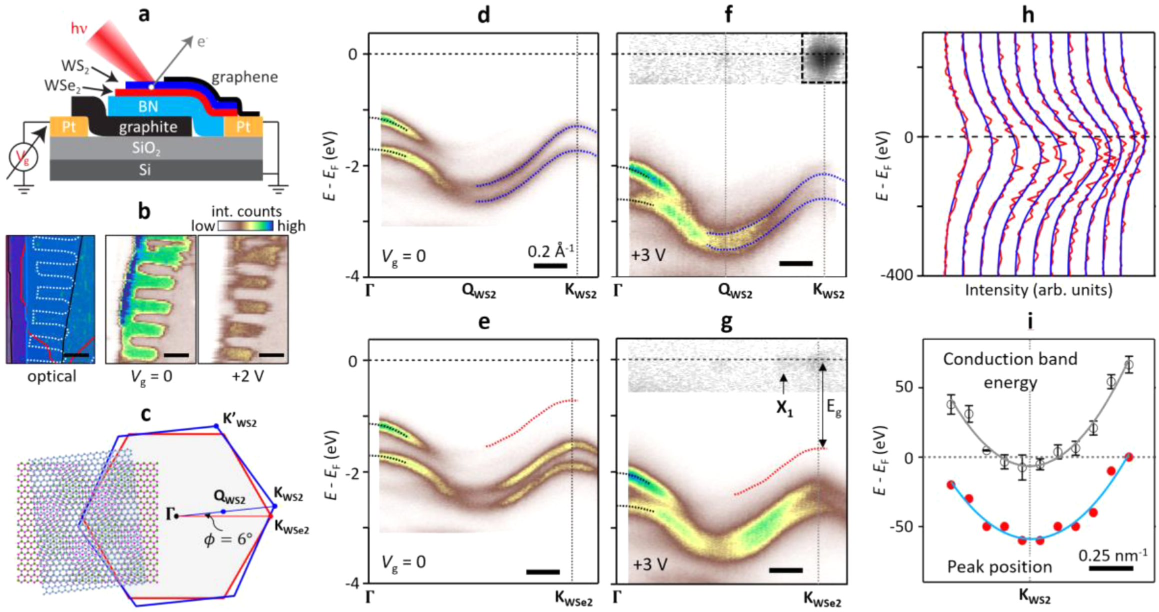

Figure 1. Valence and conduction bands in WS$_2$/WSe$_2$ moiré heterobilayer device 1, twist angle $\phi = 6°$. (a) Schematic of a device and the μARPES measurement. (b) Optical image (left) and integrated photoemission maps at labeled V_g (right) of the same region of a device (SI Sec. 4). Overlaid lines denote edges of WS$_2$ (blue), WSe$_2$ (red), the graphene top contact (dashed white), and the graphite back gate (black). At V_g = +2 V, photoemission is seen only between the graphene comb teeth. Scale bars: 10 μm. (c) Schematics of the structure and Brillouin zones of a WS$_2$/WSe$_2$ bilayer with a 6° twist. Blue and red indicate WS$_2$ and WSe$_2$, respectively. (d) and (e) Energy−momentum slices along $\mathbf{\Gamma} - \mathbf{K}_{\mathrm{WS}_2}$ and $\mathbf{\Gamma} - \mathbf{K}_{\mathrm{WSe}_2}$, respectively, at $V_g = 0$. (f) and (g) Similar measurements at V_g = +3 V. Dotted lines in (d) and (e) are fits to the WS$_2$-like bands (blue) and the WSe$_2$-like bands (red; only the upper branch is visible) near the zone boundary and to the hybridized bands near $\mathbf{\Gamma}$ (black). The same fits are overlaid and shifted vertically in parts f and g to best match the data. Intensity near E_F is plotted in a logarithmic grayscale. (h) EDCs (red) at a series of fixed momenta equally spaced across the range of the dashed box in (f). Each trace is averaged over a 0.01 Å^{-1} momentum interval and fitted with the product of a Gaussian and a Fermi function (blue lines). (i) Energy of peak photoemission intensity (solid red circles) and conduction band energy (empty black circles) extracted from the data in (h). The blue and gray parabolas are least-squares fits.

superlattice. We consider the expected relative contributions of such moiré potential-induced reconstruction of the CB states and of "final-state diffraction" of photoemitted electrons by the moiré potential as they exit the material, concluding that the CB state reconstruction effect should be dominant at small twist angles. We note that the replicas display a pronounced alternation of intensity when tracing them around the K-point, breaking the 6-fold symmetry one would expect for scattering of a free particle off a triangular or honeycomb lattice. For a model starting with circularly symmetric dispersion, as appropriate for energies near the bottom of the WS$_2$ conduction band, we show that such an intensity pattern with reduced rotational symmetry cannot be produced within a model that incorporates a purely scalar moiré potential. Our results thus reveal a significant influence of the moiré pseudovector potential that is expected to be present as a result of strain.

Devices were fabricated by mechanical exfoliation, dry transfer, and electron-beam patterning of metal electrodes as in previous work.[31] A graphene top contact, preshaped into a comb-like pattern using atomic force microscope (AFM)-based electrochemical patterning,[37] overlaps the heterobilayer which lies on a thin flake of insulating hexagonal boron nitride (hBN) over a graphite back gate, supported in turn on a SiO$_2$/Si chip (see Figure 1a and Supporting Information section 1, SI Sec. 1). Each semiconductor heterobilayer was constructed by placing monolayer flakes with their straight edges subtending a target angle. The actual angles obtained were determined from the μARPES spectra via identification of the constituent layers' valence band edges at their zone corners but could be inferred from the moiré period revealed by piezo-force microscopy[38] (PFM; see SI Sec. 2).

The lattice constants of relaxed monolayers WS$_2$ and WSe$_2$ are a_{WS_2} = 0.315 nm and a_{WSe_2} = 0.328 nm, respectively, and the lattice mismatch parameter is $\delta = (a_{\mathrm{WSe}_2}/a_{\mathrm{WSe}_2}) - 1 = 0.041$. The moiré lattice constant,[39] $a_{\mathrm{m}} = a_{\mathrm{WSe}_2}[2(1+\delta)(1-\cos\phi)+\delta^2]^{-1/2}$, has its largest value of $a_{\mathrm{WSe2}}/\delta \approx 8$ nm[16] at $\phi = 0$. On device 1, photoluminescence measurements (SI Sec. 3) show enhancements in intensity at gate voltages corresponding to the integer filling of a moiré unit cell of area consistent with the twist angle independently inferred by PFM ($a_{\mathrm{m}} \approx 2.8$ nm, $\phi = 6°$). Note that we cannot tell whether the stacking is closer to the antiparallel (centrosymmetric) or parallel (polar) configuration at $\phi = 0$ from any of these measurements.

For μARPES measurements, a device would be mounted on the temperature stage at ∼100 K with the top graphene connected to ground through a current amplifier and a voltage of V_g applied to the back gate. At high V_g, photoemission near the Fermi level E_F from the semiconductors could be obtained only when the submicrometer beam spot (27 eV photon energy) is focused between the teeth of the graphene comb, as illustrated in Figure 1b (see SI Sec. 4 for details).

Figure 1c is a sketch of the Brillouin zones for the heterobilayer in device 1. Figure 1d,e shows energy−momentum slices measured at $V_g = 0$ along the high-symmetry directions $\mathbf{\Gamma} - \mathbf{K}_{\mathrm{WS}_2}$ and $\mathbf{\Gamma} - \mathbf{K}_{\mathrm{WSe}_2}$, respectively. As usual, we plot the energy relative to E_F, i.e., $E - E_F$ (Methods). The bands near the zone corner closely match the spin-split valence bands (VBs) of isolated WS_2 and WSe_2 monolayers (see SI Sec. 5 for spectra from the corresponding monolayers), implying weak hybridization far from **Γ**, as expected. The overlaid dotted lines are fits to the upper WSe_2-like band (red) and the upper and lower WS_2-like bands (blue), yielding hole effective masses of 0.47 ± 0.02 m_e, 0.38 ± 0.01 m_e, and 0.56 ± 0.01 m_e, respectively (m_e is the free electron mass). The WS_2 spin−orbit splitting is $\Delta_{SO}^{WS_2} = 0.44 \pm 0.04$ eV, the same as in the monolayer.[40−42] The VB edge is the WSe_2-like band at $\mathbf{K}_{WSe_2}$, which is 0.58 ± 0.04 eV above the WS_2-like band maximum at $\mathbf{K}_{WS}$. These band parameters do not vary noticeably with twist angle (SI Sec. 6). When the WS_2 is on top, the WS_2-like bands near the zone boundary are more intense; this is explained by weak interlayer hybridization and the rapid falloff of photoemission strength with depth. Indeed, when the WSe_2 is on top, the converse is seen (see SI Sec. 7). In contrast, near **Γ** two bands with similar intensity are seen; this is explained by strong interlayer hybridization at **Γ**.[25]

Figure 1f,g shows corresponding measurements made at a positive voltage $V_g = +3$ V, which capacitively induces electron doping $n_g = (6.4 \pm 0.4) \times 10^{12}$ cm^{-2} (SI Sec. 1). Photoemission can now be seen from the CB edge near the E_F. Note that there is a broadening of all features relative to the $V_g = 0$ data, which can be explained by the varying electrostatic potential over the beam spot associated with the in-plane current flow that is required to replenish the photoemitted charge. Strong CB emission is seen at $\mathbf{K}_{WS_2}$ in Figure 1d, while much weaker emission is seen at $\mathbf{Q}_{WS_2}$ implying that the CB minimum at $\mathbf{Q}_{WS_2}$ is close to but higher than the one at $\mathbf{K}_{WS_2}$ (by ∼10−20 meV; see SI Sec. 1). The absolute band gap at this doping is $E_g = 1.58 \pm 0.03$ eV, while the intralayer gap between the WS_2-like bands at $\mathbf{K}_{WS_2}$ is 2.04 ± 0.03 eV, consistent with the gap of monolayer WS_2 measured at $n_g = (1.0 \pm 0.2) \times 10^{12}$ cm^{-2} in prior work.[31] These CB parameters, like the VB ones mentioned above, did not vary detectably with twist angle (SI Sec. 6).

In Figure 1g, we discern an additional spot of emission near the Fermi energy, labeled $\mathbf{X}_1$, that does not correspond to the band edge of the constituent monolayer. Figure 2 is a constant-energy map at $E = E_F$ in which $\mathbf{X}_1$ is seen as one of three satellite spots situated near the corners of a hexagon centered on $\mathbf{K}_{WS_2}$. The two others are labeled $\mathbf{X}_2$ and $\mathbf{X}_3$. These spots appear at E_F simultaneously with the CB minimum at $\mathbf{K}_{WS_2}$, as illustrated by the momentum slice passing through $\mathbf{K}_{WS_2}$ and $\mathbf{X}_2$ shown in the upper inset. To within the uncertainty, they are displaced from $\mathbf{K}_{WS_2}$ by moiré reciprocal lattice vectors $\mathbf{G}_m$. The latter are determined by the relation $\mathbf{G}_m = \mathbf{G}_{WSe_2} - \mathbf{G}_{WS_2}$, where $\mathbf{G}_{WSe_2}$ and $\mathbf{G}_{WS_2}$ are reciprocal lattice vectors of the two layers, as illustrated in the lower inset. In this device, $\mathbf{G}_m = 2\pi/a_m = 2.5$ nm^{-1}. The corresponding value of $a_m = 2.5$ nm was confirmed by PFM imaging of the device. We deduce that the satellite spots are replicas of the CB minimum related to the moiré pattern. Similar moiré-related replicas of the VB have been reported in the photoemission from WSe_2 under graphene[43] and WS_2 under graphene[44] and interpreted in terms of miniband formation.

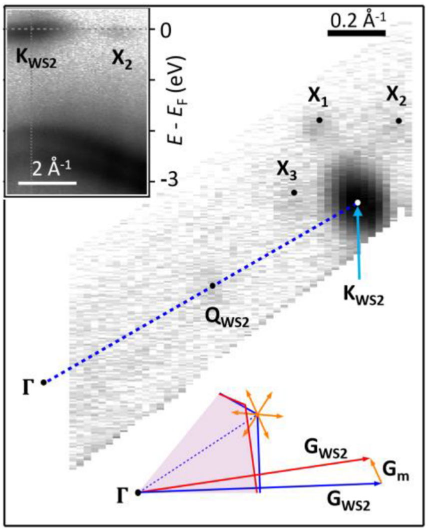

Figure 2. Moiré replicas of the conduction band in device 1. Main: photoemission intensity (on the logarithmic scale) at the Fermi energy for $V_g = +3$ V. Observable replicas of the $\mathbf{K}_{WS_2}$ conduction band are labeled $\mathbf{X}_1$, $\mathbf{X}_2$, and $\mathbf{X}_3$. Lower inset: part of the Brillouin zones of the two layers showing the construction of a moiré reciprocal lattice vector, $\mathbf{G}_m$, and a "moiré star" (orange arrows) of 6-fold counterparts of $\mathbf{G}_m$ centered on $\mathbf{K}_{WS_2}$. Upper inset: energy-momentum slice along the line through $\mathbf{K}_{WS2}$ and $\mathbf{X}_2$.

Whereas in all of our other measurements the CB edge appeared only as a shapeless blob, in the case of device 1 the combination of strong gate doping and energy resolution was sufficient for the curvature of the CB to be unambiguously apparent. Figure 1h shows energy dispersion curves (EDCs) through the CB feature in the dashed box in the top right corner of Figure 1f. The energy where the intensity is maximized, plotted as solid red circles in Figure 1h, passes through a minimum at $\mathbf{K}_{WS_2}$. The spin splitting of the CB is several times k_BT at 100 K,[40,45] so we assume that the lower spin branch is mainly populated and we derive its dispersion by fitting the EDC at each momentum to the product of a Fermi function (T = 100 K, E_F = 0) and a Gaussian (width 160 meV), treating the Gaussian center E_c as a fitting parameter (see SI Sec. 1). The resulting E_c values are plotted as open circles in Figure 1i. Fitting a parabola (black line) yields an effective mass $m_e^* = 0.15 \pm 0.02$ m_e. We note that this is substantially smaller than first-principles predictions for monolayer WS_2,[40,46] which lie in the range of 0.24−0.27 m_e.

Replicas of the CB were also seen in device 2 ($\phi \approx 2°$, $\mathbf{G}_m$ = 0.9 nm^{-1}). Figure 3a is an energy-momentum slice from the heterobilayer in device 2 along $\mathbf{\Gamma} - \mathbf{K}_{WS_2}$ at $V_g = +2.5$ V ($n_g = (4.2 \pm 0.4) \times 10^{12}$ cm^{-2}), and Figure 3b is a constant-energy map around $\mathbf{K}_{WS_2}$ at $E = E_F$. The CB feature here has three lobes that are consistent with partially resolved replicas of a central spot displaced by three moiré reciprocal lattice vectors, one of which is constructed in Figure 3c. Notably, replicas were also seen in the spectrum of graphene overlapping the heterobilayer. Its Brillouin zone (rotated by 19° relative to WS_2) is also shown in Figure 3c. Figure 3d shows an energy−momentum slice through the graphene zone corner, $\mathbf{K}_g$, and Figure 3e shows the corresponding constant-energy maps at the indicated energies. In addition to the ordinary Dirac cone centered at $\mathbf{K}_g$, there is a set of replicas around it that form a slightly distorted triangular array. The same three moiré vectors match the heterobilayer CB replicas in Figure 3b and

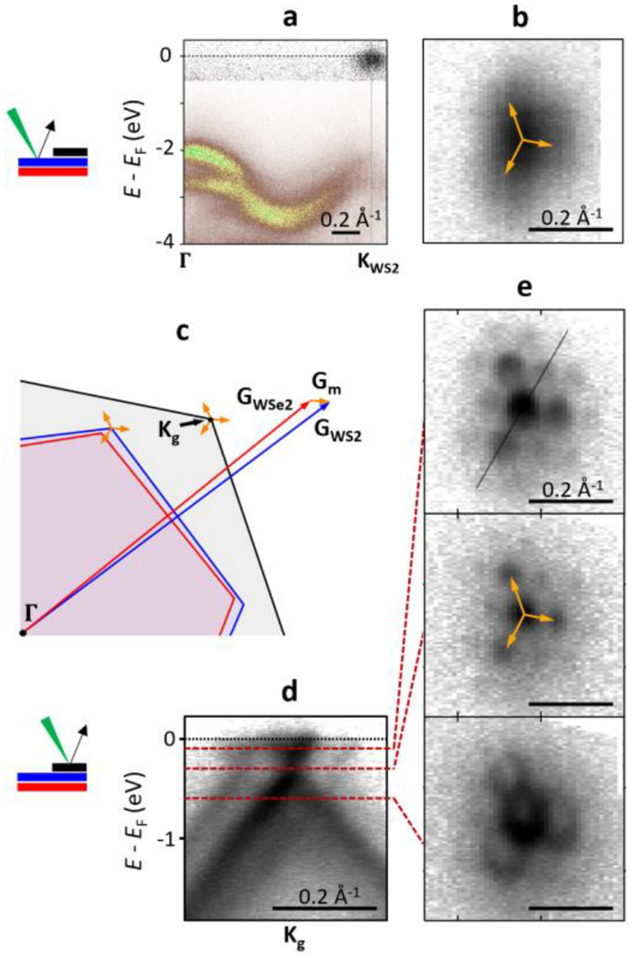

Figure 3. Moiré replicas in device 2, with twist angle $\phi = 2°$. All data were taken at $V_g = +2.5$ V. (a) Momentum slice along $\mathbf{\Gamma} - \mathbf{K}_{WS_2}$ in the WS_2/WSe_2 region (between the graphene comb teeth). (b) Constant-energy map centered on $\mathbf{K}_{WS_2}$ at E_F, averaged over 0.4 eV. Color indicates the linear scale, and grayscale indicates the logarithmic intensity scale. (c) Brillouin zones of the WS_2 (blue), WSe_2 (red), and overlapping graphene (gray), showing the construction of one of the three moiré vectors, $\mathbf{G}_m$, that are superimposed (orange) on panels (b) and (e). (d) Momentum slice through the graphene zone corner $\mathbf{K}_g$ in the graphene/WS_2/WSe_2 region. (e) Constant-energy maps centered on $\mathbf{K}_g$ at binding energies indicated by dashed red lines, $E - E_F = -0.10$, -0.25, and -0.55 eV, each averaged over 0.1 eV. The location of the slice in (d) is shown as a solid black line in the top panel of (e).

the more intense graphene replicas in Figure 3e, implying that all are related to the WS_2/WSe_2 moiré pattern. In the graphene spectra, the orientation of the "dark corridors"[47] is the same for the primary and replica bands, consistent with intravalley moiré scattering but precluding Umklapp scattering as their origin. Similar patterns were seen before in ARPES measurements[48] on (ungated) graphene on WS_2/WSe_2, where the authors also pointed out that the distortion could be due to anisotropic strain. We saw a similar pattern again in measurements on graphene overlapping a $WS_2/MoSe_2$ heterobilayer (SI Sec. 8).

In higher-twist device 3 ($\phi = 9°$, $\mathbf{G}_m = 3.6$ nm^{-1}; see SI Sec. 9) no CB replicas were visible. On the other hand, this device was the only one that exhibited VB replicas (see SI Sec. 10). This could be just a matter of energy resolution: for example, we estimate[49] that for $\phi = 6°$ a resolution of at least ∼100 meV is needed to distinguish VB replicas compared with ∼400 meV for CB replicas because of the smaller dispersion of the VB. We note that the resolution here (∼200 meV) is limited by sample quality and not instrument resolution. Our measurements do not preclude the existence of moiré bands around $\mathbf{\Gamma}$, as previously observed in twisted bilayer WSe_2.[50] Under no conditions did we see replicas associated with moiré wavevectors of the graphene/WS_2 interface where the large lattice mismatch should make moiré modulations very small. This argues in favor of a role for scattering from the moiré potential.

All of the replica features mentioned above appear to be copies of the parent bands translated by reciprocal lattice vectors of the moiré pattern of the heterobilayer. In general, these replicas result from the combination of moiré potential-induced modifications of the system's Bloch states ("initial-state modification" or "miniband formation"), as indicated schematically in Figure 4a, and scattering of the photoexcited electrons by the moiré potential as they leave the sample ("final-state diffraction"),[51−55] as indicated in Figure 4b. We now briefly discuss the qualitative features of these two contributions and the factors that point to initial-state modification as the dominant source of the replicas in devices 1 and 2. Our discussion applies both to replicas seen in the CB of WS_2 and to those observed for the graphene on top of the WS_2/WSe_2 heterostructure as seen in Figure 3.

Initial-state modification results from electrons coherently scattered on the moiré potential. New Bloch states of the superlattice are formed by hybridizing states in the original bands of the material at crystal momentum values offset by integer linear combinations of the moiré reciprocal lattice vectors $\{\mathbf{G}_m\}$; see Figure 4c (where we show the six shortest $\mathbf{G}_m$). From perturbation theory, it is straightforward to see that this hybridization is strongest when the energy differences between states offset by a moiré wavevector are small (compared with the strength of the effective moiré potential, $|U|$). Thus, initial state modification is stronger when the moiré reciprocal lattice vectors are shorter, that is, for smaller twist angles. Indeed, the CB replicas are strongest in device 2 ($\phi = 2°$; Figure 3), weaker in device 1 ($\phi = 6°$; Figure 2), and not detectable in device 3 ($\phi = 9°$).

The magnitudes of the final-state diffraction contributions are determined by the corresponding differential cross sections for the photoemitted electrons to scatter from the moiré potential. Although the interaction between the photoemitted electron and the material may be strong, due to the emitted electron's high velocity, the interaction time is short. In terms of the moiré potential amplitude U (see below for further microscopic details), the amplitude corresponding to the scattering process is controlled by the parameter $Ud/(\hbar v_{out})$, where v_{out} is the velocity of the emitted electron and d is the distance over which the moiré potential acts. For $Ud/(\hbar v_{out}) \ll 1$, the scattering amplitude may be estimated as $\mathcal{A}_{fin} \approx Ud/(\hbar v_{out})$. For comparison, consider an electronic state at momentum $\mathbf{k}$ (in the absence of the moiré potential); in the presence of the moiré potential, the wave function of this state obtains a component at momentum $\mathbf{k} + \mathbf{G}_m$ that in the perturbative regime can be estimated as $\mathcal{A}_{ini} \approx \frac{U}{[\varepsilon(\mathbf{k}) - \varepsilon(\mathbf{k}+\mathbf{G}_m)]}$ where $\varepsilon(\mathbf{k})$ is the electronic dispersion. Crucially, $\mathcal{A}_{ini}$ grows large for small $|\mathbf{G}_m|$, while $\mathcal{A}_{ini}$ is insensitive to $|\mathbf{G}_m|$ in this limit. For small twist angle ϕ (small $|\mathbf{G}_m|$) and moderate-

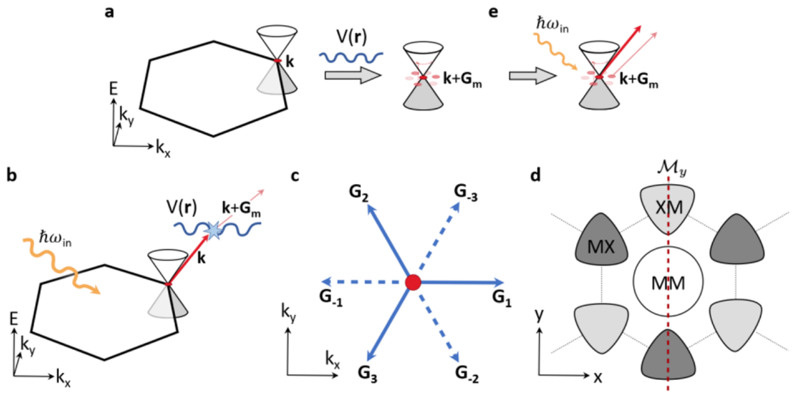

Figure 4. Origin of the moiré replicas. Illustrations with Dirac cones represent the behavior within the graphene layer on top of the WS_2/WSe_2 heterostructure, but the same mechanisms apply for the WS_2 layer. (a) Initial-state modification: Bloch states of the superlattice associated with the moiré potential $V(\mathbf{r})$ are formed from the superpositions of states in the unperturbed CB, offset by wavevectors of the moiré pattern, $\{\mathbf{G}_\mathrm{m}\}$. Photoemission from the superlattice Bloch states thus carries in-plane momentum contributions from both a central peak corresponding to the original CB and satellites (replicas) of weaker intensity that map out the momentum space structure of the reconstructed CB. (b) Final-state diffraction: Ignoring the effects of the moiré superlattice on the CB states themselves, the moiré potential may also scatter photoemitted electrons during their escape from the material, producing replica intensity spots displaced from the main peak by moiré wavevectors. As described in the text and SI Sec. 12, for small twist angles and high photoexcitation energies, we expect the observed replica intensity to be dominated by the initial state modification effect. (c) The six shortest wavevectors of the C_3-symmetric moiré pattern. (d) Schematic representation of the moiré unit cell of the WS_2/WSe_2 heterostructure with C_{3v} symmetry. The shading indicates different values of the scalar moiré potential $U(\mathbf{r})$ near the high-symmetry regions MM where the metal (W) atoms are vertically aligned and the MX (XM) regions where the metal atom of one layer sits directly above (below) the chalcogen atom of the opposite layer.

energy outgoing electrons, $\mathcal{A}_\mathrm{ini}/\mathcal{A}_\mathrm{fin} \gg 1$, the contribution from initial state modification is expected to be the dominant source of moiré replica intensity in the ARPES spectrum.

In situations where the photoemitted electrons originate from a lower monolayer and pass through an upper monolayer, we often observe replicas that are best explained by the final-state diffraction from the lattice of the upper layer. For example, in device 3 ($\phi = 9°$) we saw replicas of the WSe_2 valence band shifted by reciprocal lattice vectors of the upper WS_2 layer (SI Sec. 9). The scattering wave vectors here are long and there is no large parameter that ensures that initial state modification dominates, while the amplitude of the scattering potential can be on the atomic scale. A collection of examples of this phenomenon that we have seen in 2D heterostructures will be presented elsewhere.

In Figure 3e, we see replicas of emission from the capping graphene matching the moiré structure of the heterobilayer beneath it. Due again to the small $|\mathbf{G}_\mathrm{m}|$ and the fact that the emission is from the topmost layer, these replicas very likely reflect the modification of the graphene Bloch states.[56] One would expect anticrossings on the same energy scale between the replicas and the original bands, which would be a clear signature of mini-band formation. The absence of anticrossings in Figure 3d could be explained by the ∼200 meV energy resolution achieved here, limited by the sample quality. It would be interesting to probe this in more detail with higher-quality samples in the future as the energy scale of the gap at the anticrossings would give further insight into the magnitude of the moiré potential.

The replicas of both the WS_2 and the capping graphene bands in Figure 3 (and in ref 48) exhibit approximate 3-fold rotational symmetry. (The intensity of the data in Figure 2 is unfortunately too weak to confirm the same effect in device 1; see SI Sec. 11.) Commonly, the moiré superlattice is modeled using a real-valued scalar potential, $U(\mathbf{r})$, with C_{3v} symmetry. Since $U(\mathbf{r})$ is real-valued and hence its Fourier components satisfy $\tilde{U}_{-\mathbf{G}_\mathrm{m}} = \tilde{U}^*_{\mathbf{G}_\mathrm{m}}$, one might expect the replica intensity pattern to have 6-fold symmetry. For example, consider a low-energy effective model for the electronic states within one valley, described by the Hamiltonian $H = \hbar v(-i\nabla\cdot\sigma) + \frac{1}{2}\Delta\sigma_z + U(r)$, where $\boldsymbol{\sigma} = (\sigma_x, \sigma_y)$ and σ_z are Pauli matrices representing the orbital pseudospin degree of freedom, v is a velocity, and Δ is a gap. In Figure 4d we show a schematic representation of $U(\mathbf{r})$ in the moiré unit cell. Using the reflection symmetry of the moiré potential across the y axis (the vertical mirror plane m_y of the C_{3v} point group), $U(x, y) = U(-x, y)$, the model Hamiltonian above is symmetric under the reflection operation $x \rightarrow -x$ followed by complex conjugation. As a result, the moiré replicas centered at $\mathbf{G}_1$ and $\mathbf{G}_{-1} = -\mathbf{G}_{-1}$ are represented with equal probability in the modified (perturbed) "initial state" centered around $k = 0$ (i.e., at the valley center). Combined with the 120° rotational symmetry of the system, this would yield a 6-fold-symmetric moiré replica pattern.

Crucially, in-plane distortions of the atomic lattice break the mirror symmetry of the system.[57] The resulting local strain fields are manifested in the low-energy effective Hamiltonian through a term of the form $-\hbar v\mathbf{A}(\mathbf{r})\cdot\boldsymbol{\sigma}$, where $A(\mathbf{r})$ is a moiré (pseudo) vector potential. Physically, this emergent vector potential captures the additional phases acquired by a Bloch wave near the center of one valley as it travels between atomic sites in the strained regions, compared to the phases acquired during hopping in the undistorted structure. The sign of the moiré pseudo vector potential is opposite in valleys $\mathbf{K}$ and $\mathbf{K}'$. This moiré vector potential perturbation breaks the m_y reflection, followed by complex conjugation symmetry of the system that on its own endows the replica intensity pattern with 6-fold rotation symmetry. The in-plane distortions of the crystal lattice thereby break this 6-fold symmetry down to a 3-fold-symmetric pattern. At higher energies where the low-energy effective model is not valid (i.e., sufficiently far from the

K point), other factors such as trigonal warping can also give a 3-fold-symmetric replica pattern even with only a scalar moiré potential $U(r)$. However, the moiré pseudovector potential-induced 6-fold symmetry breaking persists even close to the K point. In SI Sec. 10 we analyze this quantitatively within the low-energy continuum model.

Underpinning much recent work on correlated and topological states in twisted semiconductor bilayers is the assumption that, far from the zone center, the bands of the two layers are only weakly hybridized and thus correspond closely to those of the separate monolayers simply superposed. Our results confirm this assumption. In the case of WS_2/WSe_2, the band alignment is such that the VB edge is at the K points in the WSe_2 layer, the CB edge is at the K points in the WS_2 layer (with the WS_2 Q-point minima just above), and the net band gap is 0.58 ± 0.03 m_e eV, all independent of the twist angle. In one sample (with a 6° twist), we made the first determination of the CB effective mass, finding it to be 0.15 ± 1 m_e (smaller than predicted). In addition, we observed replicas of the CB shifted in momentum by moiré wavevectors. After theoretically considering the relative contributions of initial-state modification and final-state diffraction, we conclude that the replicas reflect the modification of the Bloch states by the moiré potential. The same goes for corresponding replicas of the Dirac cones seen in graphene capping the bilayers. Finally, we consistently observed 3-fold (as opposed to 6-fold) symmetry of the replica pattern, which implies that the pseudovector potential, and therefore periodic strain, plays a vital role in modifying the Bloch states in moiré structures.

■ ASSOCIATED CONTENT

Data Availability Statement

Data presented in this letter are available on request from the authors.

Supporting Information

The Supporting Information is available free of charge at https://pubs.acs.org/doi/10.1021/acs.nanolett.3c04866.

Description of methods; piezo-force microscopy images; photoluminescence and reflectance measurements; optical, SPEM, and SPIM images; comparison to monolayer spectra; twist angle dependence of band structure; spectra from WSe_2 on WS_2; graphene Dirac cone replicas on $WS_2/MoSe_2$ heterobilayer; spectra from the WS_2/WSe_2 heterobilayer with a 9° twist; search for valence band replicas at a 2° twist; moiré replica intensities at 2 and 6° twists; perturbation theory for the modification of the Bloch states by the moiré potential; determining band shifts, carrier concentrations, photocurrent, and the conduction band minimum (PDF)

■ AUTHOR INFORMATION

Corresponding Authors

Xiaodong Xu – *Department of Physics, University of Washington, Seattle, Washington 98195, United States; Department of Materials Science and Engineering, University of Washington, Seattle, Washington 98195, United States;* orcid.org/0000-0003-0348-2095; Email: xuxd@uw.edu

Neil R. Wilson – *Department of Physics, University of Warwick, Coventry CV4 7AL, U.K.;* orcid.org/0000-0002-2592-3077; Email: neil.wilson@warwick.ac.uk

David H. Cobden – *Department of Physics, University of Washington, Seattle, Washington 98195, United States;* Email: cobden@uw.edu

Authors

Abigail J. Graham – *Department of Physics, University of Warwick, Coventry CV4 7AL, U.K.*

Heonjoon Park – *Department of Physics, University of Washington, Seattle, Washington 98195, United States;* orcid.org/0000-0002-3895-9589

Paul V. Nguyen – *Department of Physics, University of Washington, Seattle, Washington 98195, United States;* orcid.org/0000-0002-2935-5820

James Nunn – *Department of Physics, University of Warwick, Coventry CV4 7AL, U.K.*

Viktor Kandyba – *Elettra – Sincrotrone Trieste, S.C.p.A, Basovizza (TS), Friuli-Venezia Giulia 34149, Italy*

Mattia Cattelan – *Elettra – Sincrotrone Trieste, S.C.p.A, Basovizza (TS), Friuli-Venezia Giulia 34149, Italy*

Alessio Giampietri – *Elettra – Sincrotrone Trieste, S.C.p.A, Basovizza (TS), Friuli-Venezia Giulia 34149, Italy*

Alexei Barinov – *Elettra – Sincrotrone Trieste, S.C.p.A, Basovizza (TS), Friuli-Venezia Giulia 34149, Italy*

Kenji Watanabe – *Research Center for Electronic and Optical Materials, National Institute for Materials Science, Tsukuba 305-0044, Japan;* orcid.org/0000-0003-3701-8119

Takashi Taniguchi – *Research Center for Materials Nanoarchitectonics, National Institute for Materials Science, Tsukuba 305-0044, Japan;* orcid.org/0000-0002-1467-3105

Anton Andreev – *Department of Physics, University of Washington, Seattle, Washington 98195, United States*

Mark Rudner – *Department of Physics, University of Washington, Seattle, Washington 98195, United States*

Complete contact information is available at: https://pubs.acs.org/10.1021/acs.nanolett.3c04866

Author Contributions

N.R.W., X.X., and D.H.C. conceived and supervised the project. P.V.N. and H.P. fabricated the samples. A.J.G., P.V.N., J.N., V.K., M.C., A.G., N.R.W., and A.B. collected μ-ARPES data. A.J.G. and P.V.N. analyzed μ-ARPES data, with input from A.B., under the supervision of N.R.W. and D.H.C. H.P. acquired photoluminescence data. K.W. and T.T. provided the hBN crystals. A.A. and M.R. provided theoretical modeling and calculations. D.H.C., N.R.W., A.J.G., H.P., P.V.N., and X.X. wrote the paper with input from all of the other authors.

Notes

The authors declare no competing financial interest.

■ ACKNOWLEDGMENTS

This research on the gated electronic spectra of 2D moiré materials was supported as part of Programmable Quantum Materials, an Energy Frontier Research Center funded by the U.S. Department of Energy (DOE), Office of Science, Basic Energy Sciences (BES), under award DE-SC0019443. N.R.W. was supported through the UK Engineering and Physical Sciences Research Council grants EP/P01139X/1 and EP/T027207/1. K.W. and T.T. were supported by the JSPS KAKENHI (grant numbers 20H00354 and 23H02052) and World Premier International Research Center Initiative (WPI), MEXT, Japan. Device fabrication made use of facilities supported by the National Science Foundation (NSF) through the UW Molecular Engineering Materials Center (MEM-C), a Materials Research Science and Engineering Center (DMR-2308979).

■ REFERENCES

(1) Cao, Y.; Fatemi, V.; Fang, S.; Watanabe, K.; Taniguchi, T.; Kaxiras, E.; Jarillo-Herrero, P. Unconventional Superconductivity in Magic-Angle Graphene Superlattices. *Nature* **2018**, *556* (7699), 43–50.

(2) Cao, Y.; Fatemi, V.; Demir, A.; Fang, S.; Tomarken, S. L.; Luo, J. Y.; Sanchez-Yamagishi, J. D.; Watanabe, K.; Taniguchi, T.; Kaxiras, E.; Ashoori, R. C.; Jarillo-Herrero, P. Correlated Insulator Behaviour at Half-Filling in Magic-Angle Graphene Superlattices. *Nature* **2018**, *556* (7699), 80–84.

(3) Nuckolls, K. P.; Oh, M.; Wong, D.; Lian, B.; Watanabe, K.; Taniguchi, T.; Bernevig, B. A.; Yazdani, A. Strongly Correlated Chern Insulators in Magic-Angle Twisted Bilayer Graphene. *Nature* **2020**, *588* (7839), 610–615.

(4) Andrei, E. Y.; MacDonald, A. H. Graphene Bilayers with a Twist. *Nat. Mater.* **2020**, *19* (12), 1265–1275.

(5) Utama, M. I. B.; Koch, R. J.; Lee, K.; Leconte, N.; Li, H.; Zhao, S.; Jiang, L.; Zhu, J.; Watanabe, K.; Taniguchi, T.; Ashby, P. D.; Weber-Bargioni, A.; Zettl, A.; Jozwiak, C.; Jung, J.; Rotenberg, E.; Bostwick, A.; Wang, F. Visualization of the Flat Electronic Band in Twisted Bilayer Graphene near the Magic Angle Twist. *Nat. Phys.* **2021**, *17* (2), 184–188.

(6) Lisi, S.; Lu, X.; Benschop, T.; de Jong, T. A.; Stepanov, P.; Duran, J. R.; Margot, F.; Cucchi, I.; Cappelli, E.; Hunter, A.; Tamai, A.; Kandyba, V.; Giampietri, A.; Barinov, A.; Jobst, J.; Stalman, V.; Leeuwenhoek, M.; Watanabe, K.; Taniguchi, T.; Rademaker, L.; van der Molen, S. J.; Allan, M. P.; Efetov, D. K.; Baumberger, F. Observation of Flat Bands in Twisted Bilayer Graphene. *Nat. Phys.* **2021**, *17*, 189–194.

(7) Kerelsky, A.; McGilly, L. J.; Kennes, D. M.; Xian, L.; Yankowitz, M.; Chen, S.; Watanabe, K.; Taniguchi, T.; Hone, J.; Dean, C.; Rubio, A.; Pasupathy, A. N. Maximized Electron Interactions at the Magic Angle in Twisted Bilayer Graphene. *Nature* **2019**, *572* (7767), 95–100.

(8) Choi, Y.; Kemmer, J.; Peng, Y.; Thomson, A.; Arora, H.; Polski, R.; Zhang, Y.; Ren, H.; Alicea, J.; Refael, G.; von Oppen, F.; Watanabe, K.; Taniguchi, T.; Nadj-Perge, S. Electronic Correlations in Twisted Bilayer Graphene near the Magic Angle. *Nat. Phys.* **2019**, *15* (11), 1174–1180.

(9) Yu, H.; Wang, Y.; Tong, Q.; Xu, X.; Yao, W. Anomalous Light Cones and Valley Optical Selection Rules of Interlayer Excitons in Twisted Heterobilayers. *Phys. Rev. Lett.* **2015**, *115* (18), 187002.

(10) Zhang, C.; Chuu, C.-P.; Ren, X.; Li, M.-Y.; Li, L.-J.; Jin, C.; Chou, M.-Y.; Shih, C.-K. Interlayer Couplings, Moiré Patterns, and 2D Electronic Superlattices in MoS 2 /WSe 2 Hetero-Bilayers. *Sci. Adv.* **2017**, 3 (1), No. e1601459.

(11) Jin, C.; Regan, E. C.; Yan, A.; Iqbal Bakti Utama, M.; Wang, D.; Zhao, S.; Qin, Y.; Yang, S.; Zheng, Z.; Shi, S.; Watanabe, K.; Taniguchi, T.; Tongay, S.; Zettl, A.; Wang, F. Observation of Moiré Excitons in WSe2/WS2 Heterostructure Superlattices. *Nature* **2019**, *567* (7746), 76–80.

(12) Alexeev, E. M.; Ruiz-Tijerina, D. A.; Danovich, M.; Hamer, M. J.; Terry, D. J.; Nayak, P. K.; Ahn, S.; Pak, S.; Lee, J.; Sohn, J. I.; Molas, M. R.; Koperski, M.; Watanabe, K.; Taniguchi, T.; Novoselov, K. S.; Gorbachev, R. V.; Shin, H. S.; Fal'ko, V. I.; Tartakovskii, A. I. Resonantly Hybridized Excitons in Moiré Superlattices in van Der Waals Heterostructures. *Nature* **2019**, *567* (7746), 81–86.

(13) Seyler, K. L.; Rivera, P.; Yu, H.; Wilson, N. P.; Ray, E. L.; Mandrus, D. G.; Yan, J.; Yao, W.; Xu, X. Signatures of Moiré-Trapped Valley Excitons in MoSe2/WSe2 Heterobilayers. *Nature* **2019**, *567* (7746), 66–70.

(14) Tran, K.; Moody, G.; Wu, F.; Lu, X.; Choi, J.; Kim, K.; Rai, A.; Sanchez, D. A.; Quan, J.; Singh, A.; Embley, J.; Zepeda, A.; Campbell, M.; Autry, T.; Taniguchi, T.; Watanabe, K.; Lu, N.; Banerjee, S. K.; Silverman, K. L.; Kim, S.; Tutuc, E.; Yang, L.; MacDonald, A. H.; Li, X. Evidence for Moiré Excitons in van Der Waals Heterostructures. *Nature* **2019**, *567* (7746), 71–75.

(15) Regan, E. C.; Wang, D.; Jin, C.; Bakti Utama, M. I.; Gao, B.; Wei, X.; Zhao, S.; Zhao, W.; Zhang, Z.; Yumigeta, K.; Blei, M.; Carlström, J. D.; Watanabe, K.; Taniguchi, T.; Tongay, S.; Crommie, M.; Zettl, A.; Wang, F. Mott and Generalized Wigner Crystal States in WSe2/WS2Moiré Superlattices. *Nature* **2020**, *579* (7799), 359–363.

(16) Tang, Y.; Li, L.; Li, T.; Xu, Y.; Liu, S.; Barmak, K.; Watanabe, K.; Taniguchi, T.; MacDonald, A. H.; Shan, J.; Mak, K. F. Simulation of Hubbard Model Physics in WSe2/WS2Moiré Superlattices. *Nature* **2020**, *579* (7799), 353–358.

(17) Ma, L.; Nguyen, P. X.; Wang, Z.; Zeng, Y.; Watanabe, K.; Taniguchi, T.; MacDonald, A. H.; Mak, K. F.; Shan, J. Strongly Correlated Excitonic Insulator in Atomic Double Layers. *Nature* **2021**, *598* (7882), 585–589.

(18) Chen, D.; Lian, Z.; Huang, X.; Su, Y.; Rashetnia, M.; Ma, L.; Yan, L.; Blei, M.; Xiang, L.; Taniguchi, T.; Watanabe, K.; Tongay, S.; Smirnov, D.; Wang, Z.; Zhang, C.; Cui, Y.-T.; Shi, S.-F. Excitonic Insulator in a Heterojunction Moiré Superlattice. *Nat. Phys.* **2022**, *18* (10), 1171–1176.

(19) Wang, X.; Xiao, C.; Park, H.; Zhu, J.; Wang, C.; Taniguchi, T.; Watanabe, K.; Yan, J.; Xiao, D.; Gamelin, D. R.; Yao, W.; Xu, X. Light-Induced Ferromagnetism in Moiré Superlattices. *Nature* **2022**, *604* (7906), 468–473.

(20) Anderson, E.; Fan, F.-R.; Cai, J.; Holtzmann, W.; Taniguchi, T.; Watanabe, K.; Xiao, D.; Yao, W.; Xu, X. Programming Correlated Magnetic States with Gate-Controlled Moiré Geometry. *Science (1979)* **2023**, *381* (6655), 325–330.

(21) Zhao, W.; Shen, B.; Tao, Z.; Han, Z.; Kang, K.; Watanabe, K.; Taniguchi, T.; Mak, K. F.; Shan, J. Gate-Tunable Heavy Fermions in a Moiré Kondo Lattice. *Nature* **2023**, *616* (7955), 61–65.

(22) Cai, J.; Anderson, E.; Wang, C.; Zhang, X.; Liu, X.; Holtzmann, W.; Zhang, Y.; Fan, F.; Taniguchi, T.; Watanabe, K.; Ran, Y.; Cao, T.; Fu, L.; Xiao, D.; Yao, W.; Xu, X. Signatures of Fractional Quantum Anomalous Hall States in Twisted MoTe2. *Nature* **2023**, 63–68.

(23) Park, H.; Cai, J.; Anderson, E.; Zhang, Y.; Zhu, J.; Liu, X.; Wang, C.; Holtzmann, W.; Hu, C.; Liu, Z.; Taniguchi, T.; Watanabe, K.; Chu, J.; Cao, T.; Fu, L.; Yao, W.; Chang, C.-Z.; Cobden, D.; Xiao, D.; Xu, X. Observation of Fractionally Quantized Anomalous Hall Effect. *Nature 2023* **2023**, 74–79.

(24) Zeng, Y.; Xia, Z.; Kang, K.; Zhu, J.; Knüppel, P.; Vaswani, C.; Watanabe, K.; Taniguchi, T.; Mak, K. F.; Shan, J. Thermodynamic Evidence of Fractional Chern Insulator in Moiré MoTe2. *Nature* **2023**, *622*, 69.

(25) Wilson, N. R.; Nguyen, P. V.; Seyler, K.; Rivera, P.; Marsden, A. J.; Laker, Z. P. L.; Constantinescu, G. C.; Kandyba, V.; Barinov, A.; Hine, N. D. M.; Xu, X.; Cobden, D. H. Determination of Band Offsets, Hybridization, and Exciton Binding in 2D Semiconductor Heterostructures. *Sci. Adv.* **2017**, 3 (2), No. e1601832.

(26) Graham, A. J.; Zultak, J.; Hamer, M. J.; Zolyomi, V.; Magorrian, S.; Barinov, A.; Kandyba, V.; Giampietri, A.; Locatelli, A.; Genuzio, F.; Teutsch, N. C.; Salazar, C.; Hine, N. D. M.; Fal'ko, V. I.; Gorbachev, R. V.; Wilson, N. R. Ghost Anti-Crossings Caused by Interlayer Umklapp Hybridization of Bands in 2D Heterostructures. *2d Mater.* **2021**, *8* (1), 015016.

(27) Coy Diaz, H.; Avila, J.; Chen, C.; Addou, R.; Asensio, M. C.; Batzill, M. Direct Observation of Interlayer Hybridization and Dirac Relativistic Carriers in Graphene/MoS2 van Der Waals Heterostructures. *Nano Lett.* **2015**, *15* (2), 1135–1140.

(28) Schmitt, D.; Bange, J. P.; Bennecke, W.; AlMutairi, A. A.; Meneghini, G.; Watanabe, K.; Taniguchi, T.; Steil, D.; Luke, D. R.; Weitz, R. T.; Steil, S.; Jansen, G. S. M.; Brem, S.; Malic, E.; Hofmann, S.; Reutzel, M.; Mathias, S. Formation of Moiré Interlayer Excitons in Space and Time. *Nature* **2022**, *608* (7923), 499–503.

(29) Zheng, H.; Wu, B.; Li, S.; Ding, J.; He, J.; Liu, Z.; Wang, C. T.; Wang, J. T.; Pan, A.; Liu, Y. Localization-Enhanced Moiré Exciton in

Twisted Transition Metal Dichalcogenide Heterotrilayer Superlattices. *Light Sci. Appl.* **2023**, *12* (1), 117.

(30) Nguyen, P. V.; Teutsch, N. C.; Wilson, N. P.; Kahn, J.; Xia, X.; Kandyba, V.; Barinov, A.; Constantinescu, G. C. C.; Hine, N. D. M.; Xu, X.; Cobden, D. H. H.; Wilson, N. R. Visualizing Electrostatic Gating Effects in Two-Dimensional Heterostructures. *Nature* **2019**, *572* (7768), 220−223.

(31) Nguyen, P. V.; Teutsch, N. C.; Wilson, N. P.; Kahn, J.; Xia, X.; Graham, A. J.; Kandyba, V.; Giampietri, A.; Barinov, A.; Constantinescu, G. C.; Yeung, N.; Hine, N. D. M.; Xu, X.; Cobden, D. H.; Wilson, N. R. Visualizing Electrostatic Gating Effects in Two-Dimensional Heterostructures. *Nature* **2019**, *572* (7768), 220−223.

(32) Muzzio, R.; Jones, A. J. H.; Curcio, D.; Biswas, D.; Miwa, J. A.; Hofmann, P.; Watanabe, K.; Taniguchi, T.; Singh, S.; Jozwiak, C.; Rotenberg, E.; Bostwick, A.; Koch, R. J.; Ulstrup, S.; Katoch, J. Momentum-Resolved View of Highly Tunable Many-Body Effects in a Graphene/HBN Field-Effect Device. *Phys. Rev. B* **2020**, *101* (20), 201409.

(33) Jones, A. J. H. H.; Muzzio, R.; Majchrzak, P.; Pakdel, S.; Curcio, D.; Volckaert, K.; Biswas, D.; Gobbo, J.; Singh, S.; Robinson, J. T.; Watanabe, K.; Taniguchi, T.; Kim, T. K.; Cacho, C.; Lanata, N.; Miwa, J. A.; Hofmann, P.; Katoch, J.; Ulstrup, S. Observation of Electrically Tunable van Hove Singularities in Twisted Bilayer Graphene from NanoARPES. *Adv. Mater.* **2020**, *32* (31), 2001656.

(34) Curcio, D.; Jones, A. J. H.; Muzzio, R.; Volckaert, K.; Biswas, D.; Sanders, C. E.; Dudin, P.; Cacho, C.; Singh, S.; Watanabe, K.; Taniguchi, T.; Miwa, J. A.; Katoch, J.; Ulstrup, S.; Hofmann, P. Accessing the Spectral Function in a Current-Carrying Device. *Phys. Rev. Lett.* **2020**, *125* (23), 1−9.

(35) Nguyen, P. V.; Teutsch, N. C.; Wilson, N. P. N. R.; Kahn, J.; Xia, X.; Graham, A. J.; Kandyba, V.; Barinov, A.; Xu, X.; Cobden, D. H.; Wilson, N. P. N. R. Field-Dependent Band Structure Measurements in Two-Dimensional Heterostructures. *Nano Lett.* **2021**, *21* (24), 10532−10537.

(36) Zhang, Y.; Yuan, N. F. Q.; Fu, L. Moiré Quantum Chemistry: Charge Transfer in Transition Metal Dichalcogenide Superlattices. *Phys. Rev. B* **2020**, *102* (20), 1−6.

(37) Li, H.; Ying, Z.; Lyu, B.; Deng, A.; Wang, L.; Taniguchi, T.; Watanabe, K.; Shi, Z. Electrode-Free Anodic Oxidation Nanolithography of Low-Dimensional Materials. *Nano Lett.* **2018**, *18* (12), 8011−8015.

(38) McGilly, L. J.; Kerelsky, A.; Finney, N. R.; Shapovalov, K.; Shih, E.-M.; Ghiotto, A.; Zeng, Y.; Moore, S. L.; Wu, W.; Bai, Y.; Watanabe, K.; Taniguchi, T.; Stengel, M.; Zhou, L.; Hone, J.; Zhu, X.; Basov, D. N.; Dean, C.; Dreyer, C. E.; Pasupathy, A. N. Visualization of Moiré Superlattices. *Nat. Nanotechnol* **2020**, *15* (7), 580−584.

(39) Yankowitz, M.; Xue, J.; Cormode, D.; Sanchez-Yamagishi, J. D.; Watanabe, K.; Taniguchi, T.; Jarillo-Herrero, P.; Jacquod, P.; LeRoy, B. J. Emergence of Superlattice Dirac Points in Graphene on Hexagonal Boron Nitride. *Nat. Phys.* **2012**, *8* (5), 382−386.

(40) Kormányos, A.; Burkard, G.; Gmitra, M.; Fabian, J.; Zólyomi, V.; Drummond, N. D.; Fal'ko, V. K · p Theory for Two-Dimensional Transition Metal Dichalcogenide Semiconductors. *2d Mater.* **2015**, *2* (2), 022001.

(41) Kosmider, K.; González, J. W.; Fernández-Rossier, J. Large Spin Splitting in the Conduction Band of Transition Metal Dichalcogenide Monolayers. *Phys. Rev. B Condens Matter Mater. Phys.* **2013**, *88* (24), 1−7.

(42) Cheng, Y. C.; Zhu, Z. Y.; Tahir, M.; Schwingenschlögl, U. Spin-Orbit-Induced Spin Splittings in Polar Transition Metal Dichalcogenide Monolayers. *EPL* **2013**, *102* (5), 57001.

(43) Xie, S.; Faeth, B. D.; Tang, Y.; Li, L.; Parzyck, C. T.; Chowdhury, D.; Zhang, Y.; Jozwiak, C.; Bostwick, A.; Rotenberg, E. Direct Observation of Distinct Minibands in Moiré Superlattices. *arXiv* **2020**, 2010.07806.

(44) Ulstrup, S.; Koch, R. J.; Singh, S.; McCreary, K. M.; Jonker, B. T.; Robinson, J. T.; Jozwiak, C.; Rotenberg, E.; Bostwick, A.; Katoch, J.; Miwa, J. A. Direct Observation of Minibands in a Twisted Graphene/WS2 Bilayer. *Sci. Adv.* **2020**, *6* (14), 1−7.

(45) Liu, G.-B.; Xiao, D.; Yao, Y.; Xu, X.; Yao, W. Electronic Structures and Theoretical Modelling of Two-Dimensional Group-VIB Transition Metal Dichalcogenides. *Chem. Soc. Rev.* **2015**, *44* (9), 2643−2663.

(46) Shi, H.; Pan, H.; Zhang, Y. W.; Yakobson, B. I. Quasiparticle Band Structures and Optical Properties of Strained Monolayer MoS2 and WS2. *Phys. Rev. B Condens Matter Mater. Phys.* **2013**, *87* (15), 1−8.

(47) Mucha-Kruczyński, M.; Tsyplyatyev, O.; Grishin, A.; McCann, E.; Fal'ko, V. I.; Bostwick, A.; Rotenberg, E.; Fal'ko, V. I.; Bostwick, A.; Rotenberg, E. Characterization of Graphene through Anisotropy of Constant-Energy Maps in Angle-Resolved Photoemission. *Phys. Rev. B* **2008**, *77* (19), 195403.

(48) Xie, S.; Faeth, B. D.; Tang, Y.; Li, L.; Gerber, E.; Parzyck, C. T.; Chowdhury, D.; Zhang, Y. H.; Jozwiak, C.; Bostwick, A.; Rotenberg, E.; Kim, E. A.; Shan, J.; Mak, K. F.; Shen, K. M. Strong Interlayer Interactions in Bilayer and Trilayer Moire Superlattices. *Sci. Adv.* **2022**, *8* (12), 1911.

(49) Graham, A. J. *Interlayer Effects Revealed in Two-Dimensional Heterostructures by Angle-Resolved Photoemission Spectroscopy*. University of Warwick, 2022. https://wrap.warwick.ac.uk/169588/.

(50) Gatti, G.; Issing, J.; Rademaker, L.; Margot, F.; De Jong, T. A.; Van Der Molen, S. J.; Teyssier, J.; Kim, T. K.; Watson, M. D.; Cacho, C.; Dudin, P.; Avila, J.; Edwards, K. C.; Paruch, P.; Ubrig, N.; Gutiérrez-Lezama, I.; Morpurgo, A. F.; Tamai, A.; Baumberger, F. Flat Γ Moiré Bands in Twisted Bilayer WSe2. *Phys. Rev. Lett.* **2023**, *131* (4), 046401.

(51) Ohta, T.; Robinson, J. T.; Feibelman, P. J.; Bostwick, A.; Rotenberg, E.; Beechem, T. E. Evidence for Interlayer Coupling and Moiré Periodic Potentials in Twisted Bilayer Graphene. *Phys. Rev. Lett.* **2012**, *109* (18), 186807.

(52) Pletikosić, I.; Kralj, M.; Pervan, P.; Brako, R.; Coraux, J.; N'Diaye, A. T.; Busse, C.; Michely, T. Dirac Cones and Minigaps for Graphene on Ir(111). *Phys. Rev. Lett.* **2009**, *102* (5), 056808.

(53) Starodub, E.; Bostwick, A.; Moreschini, L.; Nie, S.; Gabaly, F. El; McCarty, K. F.; Rotenberg, E. In-Plane Orientation Effects on the Electronic Structure, Stability, and Raman Scattering of Monolayer Graphene on Ir(111). *Phys. Rev. B Condens Matter Mater. Phys.* **2011**, *83* (12), 1−9.

(54) Rotenberg, E.; Bostwick, A. Superlattice Effects in Graphene on SiC(0001) and Ir(111) Probed by ARPES. *Synth. Met.* **2015**, *210*, 85−94.

(55) Mucha-Kruczynski, M.; Wallbank, J. R.; Fal'ko, V. I. Moiré Miniband Features in the Angle-Resolved Photoemission Spectra of Graphene/ h BN Heterostructures. *Phys. Rev. B Condens Matter Mater. Phys.* **2016**, *93* (8), 085409.

(56) Xie, S.; Faeth, B. D.; Tang, Y.; Li, L.; Gerber, E.; Parzyck, C. T.; Chowdhury, D.; Zhang, Y.-H.; Jozwiak, C.; Bostwick, A.; Rotenberg, E.; Kim, E.-A.; Shan, J.; Mak, K. F.; Shen, K. M. Strong Interlayer Interactions in Bilayer and Trilayer Moiré Superlattices. *Sci. Adv.* **2022**, *8* (12), 4−10.

(57) Vitale, V.; Atalar, K.; Mostofi, A. A.; Lischner, J. Flat Band Properties of Twisted Transition Metal Dichalcogenide Homo- and Heterobilayers of MoS 2, MoSe 2, WS 2 and WSe 2. *2d Mater.* **2021**, *8* (4), 045010.